

The Impact of New Polarization Data from Bonn, Mainz and Jefferson Laboratory on $\gamma p \rightarrow \pi N$ Multipoles

A.V. Anisovich^{1,2}, R. Beck^{1a}, M. Döring^{3,4}, M. Gottschall¹, J. Hartmann¹, V. Kashevarov⁵, E. Klempt¹, Ulf-G. Meißner^{1,6,7}, V. Nikonov^{1,2}, M. Ostrick⁵, D. Rönchen^{1,6b}, A. Sarantsev^{1,2}, I. Strakovsky³, A. Thiel¹, L. Tiator⁵, U. Thoma¹, R. Workman³, Y. Wunderlich¹

¹Helmholtz-Institut für Strahlen- und Kernphysik der Universität Bonn, Nußallee 14-16, 53115 Bonn, Germany

²NRS "Kurchatov Institute", PNPI, 188300, Gatchina, Russia

³Department of Physics, George Washington University, 725 21st Street, NW, Washington, DC 20052, USA

⁴Thomas Jefferson National Accelerator Facility, 12000 Jefferson Avenue, Newport News, VA, USA

⁵Institut für Kernphysik der Universität Mainz, Johann-Joachim-Becher-Weg 45, 55099 Mainz, Germany

⁶Bethe Center for Theoretical Physics, Universität Bonn, 53115 Bonn, Germany

⁷Institut für Kernphysik, Institute for Advanced Simulation, Jülich Center for Hadron Physics, JARA FAME and JARA HPC, Forschungszentrum Jülich, 52425 Jülich, Germany

Received: date / Revised version: date

Abstract. New data on pion-photoproduction off the proton have been included in the partial wave analyses Bonn-Gatchina and SAID and in the dynamical coupled-channel approach Jülich-Bonn. All reproduce the recent new data well: the double polarization data for E , G , H , P and T in $\gamma p \rightarrow \pi^0 p$ from ELSA, the beam asymmetry Σ for $\gamma p \rightarrow \pi^0 p$ and $\pi^+ n$ from Jefferson Laboratory, and the precise new differential cross section and beam asymmetry data Σ for $\gamma p \rightarrow \pi^0 p$ from MAMI. The new fit results for the multipoles are compared with predictions not taking into account the new data. The mutual agreement is improved considerably but still far from being perfect.

1 Introduction

QCD, Quantum Chromodynamics, is the accepted theory of the strong interactions. However, the spectrum of the strongly interacting particles, the hadrons, remains to be derived from the basic principles of QCD. A good guide to the hadron spectrum has been the quark model, which include some of the basic features of QCD like the modelling of the confining force. These can thus be used to estimate the expected number of states in a given energy range. While in the meson spectrum one observes more states than given by simple quark-antiquark models, see e.g. Refs. [1,2,3], the situation is very different in the baryon sector: there are many more three-quark states predicted (see e.g. [4,5,6]) than observed. This is often called the *missing resonance* problem. Lattice QCD seems to confirm the large number of predicted states, even though these calculations use a quark mass corresponding to $m_\pi = 396$ MeV and decay properties of these states are not investigated [7]. A more recent study of baryons with $J^P = 1/2^\pm, 3/2^\pm$ varied the pion mass between 255 and 596 MeV and found good agreement with low-lying existing states [8]. Furthermore, the first lattice

QCD calculation of pion-nucleon scattering in the $J^P = 1/2^-$ channel can be found in Ref. [9]. The prediction of hybrid baryons increases the number of expected resonances even further [10,11]. Several alternatives have been suggested to understand the problem of the *missing resonances*. Here, we just mention the quark-diquark model, [12], the dynamically generation of baryon interaction of mesons and octet or decuplet (ground-state) baryons, see e.g. [13,14,15,16,17,18], the AdS/QCD model [19,20,21] or Schwinger-Dyson models [22,23]. Recent surveys of the field can be found in [24,25,26,27].

A realistic alternative solution of the problem of *missing resonances* is the possibility that these resonances have escaped observation due to a small πN coupling. In πN elastic scattering, this coupling constant enters in the entrance and the exit channel, and resonances with weak πN coupling remain unobserved. To remedy this situation, experiments have been and are being performed at Bonn [28], Mainz [29], and Newport News [30] in which high-energy photons induce reactions off nucleons. In the case of photoproduction of pseudoscalar mesons, several (at least eight) independent observables with different settings of beam and target polarization and with detection of the recoil polarization of the outgoing nucleon need to be measured to define the four complex amplitudes governing the

^a Correspondence to: beck@hiskp.uni-bonn.de

^b Correspondence to: roenchen@hiskp.uni-bonn.de

reaction [31,32,33]. For an analysis aiming to determine the partial waves of lowest angular momenta, fewer observables are sufficient provided the statistical power of the experiments is sufficiently high [34]. For example, in the region below the 2π threshold, the Watson theorem provides an additional constraint which reduces the number of necessary observables. It has been shown that a measurement of the differential cross section $d\sigma/d\Omega$ and of the photon beam asymmetry Σ in π^0 photoproduction are sufficient to determine the electric contribution (or the E2/M1 ratio) to the (dominantly magnetic) $\Delta(1232)3/2^+$ excitation [35,36]. Additional data on the polarization observable E [37], G [38] and on T , P , and H [39], allowed for a determination of a D-wave amplitude exciting the $N(1520)3/2^-$.

The four complex amplitudes for pion photoproduction are determined for each bin in energy and angle. For each of these bins, one overall phase remains undetermined. This phase is therefore generally allowed to vary with energy and angle. Hence, multipoles cannot be extracted from the four complex amplitudes (known up to the overall phase), since the angular variation of the phase prohibits the calculation of the partial wave projection integrals needed for this purpose. Instead, (model-dependent) multipoles can be determined directly in a truncated partial wave analysis, utilizing the full angular distributions of the polarization observables [40]. Then, there remains one unknown overall phase, which now depends only on the energy [41]. The multipoles obtained from such an analysis can be fitted within models which return the wanted quantities: masses, widths, the helicity amplitudes of the contributing resonances, and the background contribution. At the resonance poles, these quantities can be uniquely defined and compared to conventional Breit-Wigner parameters [42]. The πN coupling constants need to be determined from fits to πN elastic scattering data.

At present, it is not yet possible to determine the four complex amplitudes uniquely for any reaction, at least not over a range from threshold to above 2 GeV in mass. Instead, (model-dependent) multipoles can be determined from a fit to the data. One of the best studied reactions is pion photoproduction off protons, i.e. $\gamma p \rightarrow \pi^0 p$ and $\gamma p \rightarrow \pi^+ n$. Several experiments with different polarization settings have been performed recently which should lead to a better determination of the multipoles. In this paper we compare the multipoles from leading partial wave analysis groups before and after inclusion of the new data. The hope (and expectation) is that the new data enforce a convergence of the different partial wave analyses, and that a more unified picture of the spectrum of N^* and Δ^* resonances will emerge.

The paper is organized as follows. In Section 2 we outline the different partial wave analysis (PWA) approaches – Bonn-Gatchina (BnGa), Jülich-Bonn (JüBo), MAID, and SAID – used to derive the multipoles. The four PWA groups exploit different data sets: MAID used the data available in 2007 only, BnGa, JüBo and SAID make extensive use of most available data on pion and photo-induced reactions. The data are listed in Section 3. The

three groups BnGa, JüBo, and SAID made new fits based on additional new polarization data; these are also listed in Section 3. In Section 4 we present the results on the photoproduction multipoles from the energy dependent fits to the data on $\gamma p \rightarrow \pi N$. The paper concludes with a discussion and a summary in Section 5.

2 The partial wave analysis

Ideally, a partial wave analysis should respect all constraints imposed by theoretical considerations like gauge invariance, analyticity, unitarity, crossing symmetry, and chiral symmetry. All reactions should be fitted simultaneously, and the program should be fast enough to allow for systematic studies. However, at the moment this is technically not achievable. A self-consistent method satisfying all (or at least most) constraints derived from theory leads to highly complex equations and requires, consequently, high computational efforts and long fitting times, like e.g. in the Jülich-Bonn approach. Alternatively, an approach that allows for fast computing enables one to change models and to test the presence of new resonances easily. In this case, approximations have to be made. In the following, the PWA models used to fit the data and the reactions they address are outlined briefly. There are many further approaches which fit photoproduction data. We mention here recent results of EBAC (Argonne-Osaka) [43], of the Gießen group [44], and of the Kent State group [45].

2.1 BnGa

The frame of the BnGa partial wave analysis code has been documented in a number of publications. The approach relies on a fully relativistically invariant operator expansion method. It combines the analysis of different reactions imposing analyticity and unitarity constraints directly. The code calculates amplitudes for the production and decay of baryon resonances and includes some u and t -channel exchange diagrams [46,47,48]. Here, we recall its main features.

Originally the partial wave amplitudes were described in the K-matrix/P-vector approach [49]. For photoproduction reactions, amplitudes representing the t and u -channel exchanges are added to the resonant part. The multipoles representing the πN elastic amplitudes are calculated exploiting a technique described in [48]. In the analysis of new data sets, new resonances with masses above 2.2 GeV were included as relativistic multi-channel Breit-Wigner amplitudes.

Recently, the K-matrix/P-vector approach was changed to a dispersion-relation approach based on the N/D technique. The real part of the two body loop diagrams was then calculated using the regularization subtraction procedure with a subtraction point taken at the channel threshold. In this simplified version, the N/D-method corresponds to the K-matrix approach with real parts of the loop diagrams taken into account. For three-body final states, only the imaginary part of the loop diagrams is taken into

account, which is calculated as the spectral three-body integral.

A multi-channel amplitude $\hat{\mathbf{A}}(s)$ with the matrix elements $A_{ab}(s)$ defines the transition amplitude from a state 'a' to state 'b' where the initial and the final channels are, e.g., γN , πN , ηN , $K\Lambda$, $\pi\Delta$. The partial wave amplitude depends on the isospin I , the total angular momentum J , and the parity P ; the quantities $I(J^P)$ are suppressed here. Transitions between different channels are taken into account explicitly in the K-matrix; the amplitude is given by

$$\hat{\mathbf{A}}(s) = \hat{\mathbf{K}} (\hat{\mathbf{I}} - \hat{\mathbf{B}}\hat{\mathbf{K}})^{-1}. \quad (1)$$

where $\hat{\mathbf{K}}$ is the K-matrix, $\hat{\mathbf{I}}$ is the unity matrix and $\hat{\mathbf{B}}$ is a diagonal matrix of the respective loop diagrams. The imaginary part of the elements B_j is equal to the corresponding phase spaces

$$\hat{B}_j = \text{Re}B_j + i\rho_j. \quad (2)$$

If the real part of the loop diagram is neglected, this method corresponds to the classical K-matrix approach. For two-particle states (for example πN), the phase space for $J = L + 1/2$ states is equal to (see [47]):

$$\rho_+(s) = \frac{\alpha_L}{2L+1} \frac{2|\mathbf{k}|}{\sqrt{s}} \frac{k_{10} + m_N}{2m_N} \frac{|\mathbf{k}|^{2L}}{F(L, r, k^2)} \quad (3)$$

and for states with $J = L - 1/2$, it is given by

$$\rho_-(s) = \frac{\alpha_L}{L} \frac{2|\mathbf{k}|}{\sqrt{s}} \frac{k_{10} + m_N}{2m_N} \frac{|\mathbf{k}|^{2L}}{F(L, r, k^2)}. \quad (4)$$

Here, s is the total energy squared, k is the relative momentum between baryon and meson, \mathbf{k} its three-vector component, k_{10} is the energy of the baryon (with mass m_N) calculated in the c.m.s. of the reaction, and L is the orbital angular momentum of the baryon-meson system. The coefficient α_L is equal to:

$$\alpha_L = \prod_{n=1}^L \frac{2n-1}{n}. \quad (5)$$

The phase volume is regularized at large energies by a standard Blatt-Weisskopf form factor normalized as $F(L, r, k^2) \rightarrow k^{2L}$ ($s \rightarrow \infty$). We use $r = 0.8$ fm as range of the interaction. The functions $F(L, r, k^2)$ are given explicitly in Ref. [46].

Using these phase-space volumes, the elements of the diagonal matrix \hat{B} are calculated as:

$$B_j(s) = b_j + (s - (m_{1j} + m_{2j})^2) \times \int_{(m_{1j} + m_{2j})^2}^{\infty} \frac{ds'}{\pi} \frac{\rho_j(s')}{(s' - s - i\varepsilon)(s' - (m_{1j} + m_{2j})^2)}, \quad (6)$$

where b_j are subtraction constants and m_{1j}, m_{2j} are masses of the particles in the channel j . The exact formulas for the three-body phase-space volume are given in [47].

The K-matrix $\hat{\mathbf{K}}$ is cast into the form

$$K_{ab} = \sum_{\alpha} \frac{g_a^{(\alpha)} g_b^{(\alpha)}}{M_{\alpha}^2 - s} + f_{ab}. \quad (7)$$

M_{α} and $g_a^{(\alpha)}$ are the mass and the coupling constant of the resonance α ; f_{ab} describes a direct (non-resonant) transition from the initial state a to the final state b , e.g. from $\pi N \rightarrow \Lambda K$. For most partial waves it is sufficient to assume that f_{ab} are constants. The S_{11} and S_{31} waves require a slightly more complicated structure, we use

$$f_{ab} = \frac{f_{ab}^{(1)} + f_{ab}^{(2)} \sqrt{s}}{s - s_0^{ab}}. \quad (8)$$

In this case, the $f_{ab}^{(i)}$ and s_0^{ab} are constants which are determined in the fits. In the case of the S_{11} wave, this more flexible parameterization is required to describe S -wave transitions $\pi N \rightarrow \pi N$, $\pi N \rightarrow \eta N$, and $\eta N \rightarrow \eta N$. This form was also tried for P -wave amplitudes but it did not improve the quality of the fit. Let us note that this form is similar to the one used by SAID [50].

The helicity-dependent photoproduction amplitude to produce the final state 'b' from the initial state 'a' is then given by

$$A_a = \hat{P}_b (\hat{I} - \hat{B}\hat{K})_{ba}^{-1}, \quad (9)$$

where the production vector \hat{P} is written in the form

$$P_b = \sum_{\alpha} \frac{g_{\gamma N}^{(\alpha)} g_b^{(\alpha)}}{M_{\alpha}^2 - s} + \tilde{f}_{(\gamma N)b}. \quad (10)$$

The coefficients $g_{\gamma N}^{(\alpha)}$ are the photo-couplings of the resonance α and the non-resonant production of a final state b is represented by $\tilde{f}_{(\gamma N)b}$. These are functions of s but in practice, constant values $\tilde{f}_{(\gamma N)b}$ are sufficient to obtain a good fit.

Due to its weak coupling, the γN interaction can be taken into account in the form of a P-vector. No loops due to virtual decays of a resonance into γN and back into the resonance are required. A similar approach can be used to describe decay modes with a weak coupling in the form of a D-vector amplitude. Then the transition from K-matrix channel a to the final channel f can be described as:

$$A_{af} = \hat{D}_{af} + [\hat{K}(\hat{I} - \hat{B}\hat{K})^{-1} \hat{B}]_{ab} \hat{D}_{bf}. \quad (11)$$

The parametrization of the D-vector follows the one for the P-vector:

$$D_{bf} = \sum_{\alpha} \frac{g_b^{(\alpha)} g_f^{(\alpha)}}{M_{\alpha}^2 - s} + \tilde{d}_{bf}. \quad (12)$$

Here, $g_f^{(\alpha)}$ is the coupling of a resonance to the final state and \tilde{d}_{bf} represents non-resonant transitions from the K-matrix channel b to the final state f . The D-vector approach is used for the channels with three-body final states

(e.g. $f_0(980)N$, $N(1535)\pi$). In the present analysis the non-resonant transitions for these final states are not needed to get a good description of the data. In cases where both initial and final coupling constants are weak, we use an approximation which we call PD-vector. In this case the amplitude is given by

$$A_f = \hat{G}_f + \hat{P}_a[(\hat{I} - \hat{B}\hat{K})^{-1}\hat{B}]_{ab}\hat{D}_{bf}. \quad (13)$$

\hat{G}_f corresponds to a tree diagram for the transition from initial channel (γN in the case photoproduction) to the state ' f ':

$$G_f = \sum_{\alpha} \frac{g_{\gamma N}^{(\alpha)} g_f^{(\alpha)}}{M_{\alpha}^2 - s} + \tilde{h}_{(\gamma N)f}. \quad (14)$$

Here, $g_{\gamma N}^{(\alpha)}$ is the resonance photoproduction coupling and $\tilde{h}_{(\gamma N)f}$ represents direct non-resonant transitions from the initial photon-nucleon system to the different final states.

At high energies, angular distributions of photo-produced mesons exhibit clear peaks in the forward direction. These peaks originate from meson exchanges in the t -channel. Their contributions are parameterized as π , $\rho(\omega)$, K or K^* exchanges. The corresponding exchange amplitudes are written in the form of the exchange of Regge trajectories. The invariant part of the t -channel exchange amplitude can then be written as [51]:

$$A = g(t) \frac{1 + \xi \exp(-i\pi\alpha(t))}{\sin(\pi\alpha(t))} \left(\frac{\nu}{\nu_0} \right)^{\alpha(t)}. \quad (15)$$

We use $g(t) = c \exp(-bt)$ as vertex function and form factor. Further, $\alpha(t)$ describes the trajectory, $\nu = \frac{1}{2}(s - u)$, ν_0 is a normalization factor, and ξ the signature of the trajectory. Note that the Pomeron, f_0 and π have a positive, whereas the ρ , ω and a_1 exchanges have a negative signature. The Reggeon propagators are written as

$$\begin{aligned} R(+, \nu, t) &= \frac{e^{-i\frac{\pi}{2}\alpha(t)}}{\sin(\frac{\pi}{2}\alpha(t))} \left(\frac{\nu}{\nu_0} \right)^{\alpha(t)}, \\ R(-, \nu, t) &= \frac{ie^{-i\frac{\pi}{2}\alpha(t)}}{\cos(\frac{\pi}{2}\alpha(t))} \left(\frac{\nu}{\nu_0} \right)^{\alpha(t)}. \end{aligned} \quad (16)$$

where '+' and '-' indicate the signature of the Regge-trajectories, '+' for natural parity exchange ($J^P = 0^+$, 1^- , 2^+ , ...) and '-' for unnatural parity exchange ($J^P = 1^+$, 2^- , 3^+ , ...). To eliminate the poles at $t < 0$ additional Γ -functions are introduced in Eq. (16). In the case of the Pomeron trajectory

$$\sin\left(\frac{\pi}{2}\alpha(t)\right) \rightarrow \sin\left(\frac{\pi}{2}\alpha(t)\right) \Gamma\left(\frac{\alpha(t)}{2}\right). \quad (17)$$

For ρ and ω exchanges the poles at $t < 0$ start from $\alpha = -1$ and therefore

$$\cos\left(\frac{\pi}{2}\alpha(t)\right) \rightarrow \cos\left(\frac{\pi}{2}\alpha(t)\right) \Gamma\left(\frac{\alpha(t)}{2} + \frac{1}{2}\right). \quad (18)$$

For pion production, e.g., we use ρ and ρ' exchanges with the following trajectories:

$$\begin{aligned} \rho : \quad \alpha(t) &= 0.5 + (0.85/GeV^2)t \\ \rho' : \quad \alpha(t) &= -0.75 + (0.85/GeV^2)t, \end{aligned} \quad (19)$$

for t given in units of GeV^2 . With these amplitudes, large data sets have been fitted. We quote here a few recent papers [52, 53, 54, 55, 56].

2.2 JüBo

The Jülich-Bonn model has been developed over the years, see Refs. [57, 58, 59, 60] and references therein. It should be noted that, strictly speaking, JüBo is not a PWA but rather a dynamical coupled-channel (DCC) approach, it also aims at a microscopic description of reaction dynamics. The JüBo approach allows to extract the baryon spectrum based on a simultaneous analysis of pion- and photon-induced reactions. Theoretical constraints of the S -matrix like unitarity and analyticity are manifestly implemented or at least approximated in case of three-body unitarity. Left-hand cuts as well as the correct structure of complex branch points are taken into account. The formalism allows for the determination of resonance states in terms of poles in the complex energy plane of the scattering matrix together with the corresponding residues and helicity couplings. Note that such a determination is independent of any assumption on the resonance line shape, such as the commonly used Breit-Wigner parameterization [42].

The scattering process of pion-induced reactions is described by a Lippmann-Schwinger equation that reads, after projection to the partial-wave basis,

$$\begin{aligned} T_{\mu\nu}(q, p', E) &= V_{\mu\nu}(q, p', W) \\ &+ \sum_{\kappa} \int_0^{\infty} dp p^2 V_{\mu\kappa}(q, p, W) G_{\kappa}(p, W) T_{\kappa\nu}(p, p', W), \end{aligned} \quad (20)$$

where μ (ν , κ) denote the outgoing (incoming, intermediate) meson-baryon channels πN , ηN , KA , $K\Sigma$ and the effective three-body channels $\pi\Delta$, σN , and ρN . The resonant sub-amplitudes in the latter channels describe the corresponding phase shifts of $\pi\pi$ and πN scattering [61, 62]. Explicit expressions for the two- and three-body propagators encoded in G_{κ} can be found in Ref. [62]. Non-analyticities from complex branch points [63] are also included. In Eq. (20), $W = \sqrt{s}$ denotes the scattering energy and $q \equiv |\mathbf{q}|$ ($p' \equiv |\mathbf{p}'|$) is the modulus of the outgoing (incoming) three-momentum that can be on- or off-shell. The scattering potential $V_{\mu\nu}$ is constructed from an effective Lagrangian using time-ordered perturbation theory. Resonance states are included in $V_{\mu\nu}$ in the form of s -channel processes, while t - and u -channel exchanges of light mesons and baryons constitute the non-resonant part of the potential, in addition to contact interaction terms [60] to simulate heavy exchanges that do not behave as dynamical degrees of freedom.

The explicit inclusion of t - and u -channel diagrams is, on the one hand, necessary to fulfill constraints from three-body unitarity [64]. On the other hand, the scattering amplitude has left-hand cuts with associated branch points. To respect these non-analyticities at the correct position, u -channel diagrams are included. The strengths of these cuts, however, cannot be derived in the JüBo framework. Therefore, the associated vertices can be varied using form factors, in order to let the data determine their strengths. For some t -channel quantum numbers (ρ, σ), however, pseudo-data for $N\bar{N} \rightarrow \pi\pi$ exist, which allows to determine their strength using crossing [61, 65]. The amplitude contains also the nucleon pole at the physical position and with the physical residue, obtained through the renormalization process described, e.g., in Ref. [60].

The potential $V_{\mu\nu}$ of Eq. (20) is written as

$$V_{\mu\nu} = \sum_{i=0}^n \frac{\gamma_{\mu;i}^a \gamma_{\nu;i}^c}{W - m_i^b} + V_{\mu\nu}^{\text{NP}} + \frac{1}{m_N} \gamma_{\mu}^{\text{CT};a} \gamma_{\nu}^{\text{CT};c}. \quad (21)$$

The first term denotes the sum of all s -channel resonance graphs in a given partial wave. The bare creation (annihilation) vertices $\gamma_{\mu;i}^c$ ($\gamma_{\nu;i}^a$) of a resonance i with bare mass m_i^b are constructed from an effective Lagrangian that can be found in Table 8 of Ref. [57]. Explicit expressions of the $\gamma_{\mu;i}^c$ and $\gamma_{\nu;i}^a$ are given in Refs. [57, 58]. Note that no SU(3) assumptions are made for the s -channel resonances. The t - and u -channel exchange diagrams comprised in V^{NP} are also derived from an effective Lagrangian and here, SU(3) flavor symmetry is used to relate the coupling constants of the different meson-baryon channels [58]. Form factors allow for (moderate) breaking of SU(3) symmetry. An overview of the various hadron exchanges included in the approach is given in Ref. [58]. The contact vertex functions $\gamma_{\mu}^{\text{CT};c}$ ($\gamma_{\nu}^{\text{CT};a}$) are described in detail in Ref. [60]. In the Jülich-Bonn approach, the dynamical generation of resonances via the interplay of the t - and u -channel terms alone, without the need for a bare resonance, is possible and realized for some resonances [58]. Note also, that the parameters of the bare resonances have no physical meaning but only the ones of the fully dressed states.

The photoproduction of pseudoscalar mesons is studied using the approach developed in Ref. [59] (for a manifestly gauge-invariant variant of the approach, see Ref. [66]). While in Ref. [59] the hadronic final-state interaction is provided by the Jülich-Bonn DCC model, the photoproduction interaction kernel is parameterized by energy-dependent polynomials, avoiding any further input from Born graphs.

The multipole amplitude $M_{\mu\gamma}$ of the photoproduction process is given by [59]

$$M_{\mu\gamma}(q, W) = V_{\mu\gamma}(q, W) + \sum_{\kappa} \int_0^{\infty} dp p^2 T_{\mu\kappa}(q, p, W) G_{\kappa}(p, W) V_{\kappa\gamma}(p, W). \quad (22)$$

Here, the index γ denotes the initial γN state and $T_{\mu\kappa}$ is the hadronic half-off-shell T -matrix introduced in Eq. (20).

The photoproduction kernel $V_{\mu\gamma}$ of Eq. (22) is written as

$$V_{\mu\gamma}(p, W) = \alpha_{\mu\gamma}^{\text{NP}}(p, W) + \sum_i \frac{\gamma_{\mu;i}^a(p) \gamma_{\gamma;i}^c(W)}{W - m_i^b}. \quad (23)$$

The vertex function $\gamma_{\gamma;i}^c$ describes the tree-level coupling of the γN channel to the nucleon and the excited baryonic states with resonance number i . The photon coupling to the non-pole part of the photoproduction kernel is represented by α^{NP} . The hadronic resonance annihilation vertex $\gamma_{\mu;i}^a$ is the same that is used in the construction of the hadronic scattering potential in Eq. (21). Note that, so far, the combined fits of hadronic scattering and photoproduction data have not led to any resonance pole that was not already present in the analysis of hadronic scattering alone, but kaon photoproduction data are not yet included.

2.3 MAID

In the spirit of a dynamical approach to pion photo- and electroproduction, the t -matrix of the unitary isobar model MAID is set up by the ansatz [67]

$$t_{\gamma\pi}(W, Q^2) = t_{\gamma\pi}^B(W, Q^2) + t_{\gamma\pi}^R(W, Q^2), \quad (24)$$

with a background and a resonance t -matrix, each of them constructed in a unitary way. Here, Q^2 defines the virtuality of the photon.

For a specific partial wave $\alpha = \{j, l, \dots\}$, the background t -matrix is set up by a potential multiplied by the pion-nucleon scattering amplitude in accordance with the K-matrix approximation,

$$t_{\gamma\pi}^{B,\alpha}(W, Q^2) = v_{\gamma\pi}^{B,\alpha}(W, Q^2) [1 + it_{\pi N}^{\alpha}(W)], \quad (25)$$

where only the on-shell part of pion-nucleon rescattering is maintained and the off-shell part from pion-loop contributions is neglected. Whereas this approximation would fail near the threshold for γ, π^0 [68, 69], it is well justified in the resonance region because the main contribution from pion-loop effects is absorbed by the nucleon resonance dressing.

The background potential $v_{\gamma\pi}^{B,\alpha}(W, Q^2)$ is described by Born terms obtained with an energy-dependent mixing of pseudovector-pseudoscalar πNN coupling and t -channel vector meson exchanges. The mixing parameters and coupling constants are determined by an analysis of nonresonant multipoles in the appropriate energy regions [70]. In the latest version MAID2007 [71], the S, P, D , and F waves of the background contributions are unitarized as explained above, with the pion-nucleon elastic scattering amplitudes, $t_{\pi N}^{\alpha} = [\eta_{\alpha} \exp(2i\delta_{\alpha}) - 1]/2i$, described by phase shifts δ_{α} and the inelasticity parameters η_{α} , are taken from the GWU/SAID analysis [72].

For the resonance contributions we follow Ref. [70] and assume Breit-Wigner forms for the resonance shape,

$$t_{\gamma\pi}^{R,\alpha}(W, Q^2) = \bar{A}_{\alpha}^R(W, Q^2) \times \frac{f_{\gamma N}(W) \Gamma_{\text{tot}}(W) M_R f_{\pi N}(W)}{M_R^2 - W^2 - iM_R \Gamma_{\text{tot}}(W)} e^{i\phi_R(W, Q^2)}, \quad (26)$$

where $f_{\pi N}(W)$ is the usual Breit-Wigner factor describing the decay of a resonance with total width $\Gamma_{tot}(W)$ and partial πN width $\Gamma_{\pi N}(W)$. The vertex functions for γN and πN and the partial widths for the πN , $\pi\pi N$ and ηN channels are parametrized in a common way, which may differ in some model-dependent parts. All details of the parametrization and fitted values are found in Ref. [71]. The phase $\phi_R(W, Q^2)$ in Eq. (26) is introduced to adjust the total phase such that the Fermi-Watson theorem is fulfilled below two-pion threshold.

The current version, MAID2007, describes all 13 four-star resonances below $W = 2$ GeV: $\Delta(1232)3/2^+$, $N(1440)1/2^+$, $N(1520)3/2^-$, $N(1535)1/2^-$, $\Delta(1620)1/2^-$, $N(1650)1/2^-$, $N(1675)5/2^-$, $N(1680)5/2^+$, $\Delta(1700)3/2^-$, $N(1720)3/2^+$, $\Delta(1905)5/2^+$, $\Delta(1910)1/2^+$, and $\Delta(1950)7/2^+$. In a coming update of MAID, this list of dominant resonances is no longer sufficient, due to the high accuracy of the data and the availability of many polarization observables with single and double polarization. With these data, also the weaker three-star and two-star resonances can be analyzed and will be included in the model.

In most cases, the resonance couplings $\bar{A}_\alpha^R(W, Q^2)$ are assumed to be independent of the total energy. However, for the $\Delta(1232)3/2^+$ it was critical to also introduce an energy dependence in terms of the virtual photon three-momentum $k(W, Q^2)$. For all other resonances discussed here, we assume a simple Q^2 dependence, $\bar{A}_\alpha(Q^2)$, parameterized as functions of Q^2 by an ansatz

$$\bar{A}_\alpha(Q^2) = \bar{A}_\alpha(0)(1 + a_1 Q^2 + a_2 Q^4 + \dots) e^{-b_1 Q^2}. \quad (27)$$

The electromagnetic couplings of the resonance excitations, $\bar{A}_\alpha^R(W, Q^2)$ are for most cases energy-independent. For real photons, $Q^2 = 0$, they are fitted to the pion photoproduction data. For virtual photons they are parametrized as functions of Q^2 and are fitted to the world data of pion electroproduction. For further details see Ref. [67, 71].

A special advantage in the MAID ansatz is that it is applicable for all isospin channels and also for electroproduction. It is fitted up to photon virtualities of $Q^2 \approx 5$ GeV², in the isoquartet $J^P = 3/2^+$ partial wave of the $\Delta(1232)3/2^+$ region even up to $Q^2 = 8$ GeV².

2.4 SAID

The SAID fit parametrization recently transitioned from a form, motivated [73] by a 3-channel Heitler K-matrix, similar to the MAID approach, to a form [74] based on the same Chew-Mandelstam K-matrix used in the SAID πN elastic scattering fits [75]. The form used in πN elastic scattering is

$$T_{\alpha\beta} = [1 - \bar{K}C]_{\alpha\sigma}^{-1} \bar{K}_{\sigma\beta}, \quad (28)$$

where the indices label channels πN , $\pi\Delta$, ρN , and ηN and C is the Chew-Mandelstam function described in Refs. [74, 75, 76, 77]. The extension used to include an electromagnetic channel is

$$T_{\alpha\gamma} = [1 - \bar{K}C]_{\alpha\sigma}^{-1} \bar{K}_{\sigma\gamma}. \quad (29)$$

The added elements $\bar{K}_{\sigma\gamma}$ provide the γN coupling to the hadronic channels. The energy dependence is parameterized in terms of an energy polynomial, similar to that used in the Jülich-Bonn analysis. For the $\gamma N \rightarrow \pi N$ channels, these elements are further constrained to approach the Born terms at threshold.

The SAID formalism differs from all other approaches described here in the way resonance properties are deduced. Only the $\Delta(1232)3/2^+$ is explicitly introduced as a Chew-Mandelstam K-matrix pole. All other poles arise from the factor $[1 - \bar{K}C]^{-1}$ which is common to the πN scattering and photoproduction analyses. Two important facts follow. First, the pion photoproduction analysis will have the same pole/cut structure as in the πN scattering analysis. Second, as the poles are generated - not added by hand - only those necessary to fit this process are produced. This is then the minimal required set.

The Chew-Mandelstam K-matrix parameters for hadronic channels are obtained from fits to the SAID πN elastic and ηN production database [78]. The K-matrix elements associated with the $\pi\Delta$ and ρN channels serve to provide quasi-two-body branch points in a unitary approach but are not fitted to reaction data. The hadronic parameters are fixed in the analysis of photoproduction data. Only the polynomial elements of $\bar{K}_{\sigma\gamma}$ in Eq. (29) have been varied in the present study.

2.5 Comparison of the methods

All partial wave analyses/dynamically coupled-channel approaches discussed here aim at representing the physical reality, however, at different levels of sophistication. All models allow for coupled channel effects. All models respect - at least approximately - two-body unitarity. And in all four approaches, the amplitudes are analytic functions of the invariant mass.

The JüBo model is a dynamical coupled-channel (DCC) model based on a hadronic scattering potential. The potential is iterated in a Lippmann-Schwinger equation formulated in time-ordered perturbation theory; two-body unitarity is thus fulfilled automatically. The three-body $\pi\pi N$ final state is represented by the channels ρN , σN and $\pi\Delta(1232)3/2^+$. t - and u -channel exchanges of known mesons and baryons are derived from an effective Lagrangian, these contributions form the non-resonant part of the amplitude. Data on pion and photo-induced reactions are fitted simultaneously, eleven N^* and ten Δ^* resonances are included in the fit, and their properties are derived from fits to the data. In addition, three dynamically generated states are found. The JüBo model is the most ambitious approach. The price one has to pay is that it requires the largest computing power.

The main focus of the BnGa model is the search for new N^* and Δ^* resonances, the so-called *missing resonances*, which are expected at masses above 1.7 GeV. Constraints governing the low-energy regime from chiral perturbation theory or from the Watson theorem are not imposed; however, the fit solution satisfies the Watson theorem to a few degrees. In the model, resonances in a

given partial wave are added in a K-matrix. The t - and u -channel exchanges are used to parametrize the main part of the background, smaller phenomenological background contributions are added within the K-matrix. The data on pion and photo-induced reactions are fitted in a common fit. The data include three-body final states which are fitted event by event in a likelihood fit. The fit determines the properties of nineteen N^* and nine Δ^* resonances. The program is optimized to yield fast response: excluding three-body final states, a few hundreds of fits can be performed to validate the existence and the quantum numbers of new states. When three-body final states are included, the number of fits is limited to a few dozens.

The MAID model uses multi-channel Breit-Wigner amplitudes to describe the resonant part of the photoproduction amplitude. The contribution of background channels (Born terms and t -channel exchanges) to the photoproduction cross section is large. The additional resonant contributions interfere destructively and bring the cross section down to the observed level. The phases of the total amplitude are modified by additional phases which are adjusted to guarantee the Watson theorem for the mass range below the 2π production. At present, the seven four-star N^* and the six four-star Δ^* resonances are included in the fit. Their masses, widths and πN couplings are taken from the RPP.

The SAID model is the only approach in which no resonances (except the $\Delta(1232)3/2^+$) are put in *a priori*. Instead, the K-matrix elements in Eq. (28) are expanded as polynomials in $W - W_{\text{threshold}}$. The K-matrix elements describe elastic and charge exchange scattering and inelastic channels like ηN , ρN , and $\pi\Delta(1232)3/2^+$. The degree of the polynomials varies with the mass range to be covered from small values up to 5. The approach is very efficient to fit real and imaginary parts of partial wave amplitudes for πN (quasi-) elastic scattering or the reaction $\pi N \rightarrow \eta N$. Photoproduction data are fitted once masses, widths, and πN couplings are known from fits to the πN data.

3 Data used in the analysis

The four partial wave analyses groups (BnGa, JüBo, MAID, SAID) use a large body of pion and photo-induced reactions. Only the SAID group fits the data on πN elastic scattering and determines in energy-independent fits the real and imaginary part of the πN partial wave amplitudes (given in slices of the invariant mass). The other three PWA groups use these amplitudes, jointly with further data, in energy-dependent fits. The *predictions* of the different PWAs resulting from fits to early data and these *predictions* are shown to the recent new data in Fig. 1. The recent new data include measurements of the beam asymmetry Σ [94,95], on T , P and H [96], G [38,97], and E [37,98] for the reaction $\gamma p \rightarrow \pi^0 p$. For the reaction $\gamma p \rightarrow \pi^+ n$, new data are available on the beam asymmetry Σ [95]. These data are (mostly) not used in the *predictions*.

SAID: The SAID group uses these partial wave amplitudes to determine masses M_i , widths Γ_i , and πN branching ratios $\text{BR}_i^{N\pi}$ of the contributing resonances [50]. In earlier fits, the full GWU/SAID data base for $\gamma p \rightarrow \pi^0 p$ and $\pi^+ n$ was used by SAID. The fits allowed for a renormalization of angular distributions, with a χ^2 penalty determined by the overall systematic error. In the new fits, this freedom was removed for the new polarized measurements [96,97,98]. A weighting factor of four in the χ^2 fit was applied to these data, while the set of previous measurements remained unweighted. The included energy range, in E_γ , was 155 MeV to 2.7 GeV, the lower limit being chosen to avoid the $\pi^+ n$ threshold. In order to avoid fitting mutually inconsistent cross section experiments from the full SAID database, a choice of relatively recent and non-overlapping cross section experiments was made for both charged and neutral pion production [83, 84, 85, 86, 87].

JüBo: JüBo [58] fits the amplitudes of the SAID WI08 energy-dependent solution jointly with data on other pion-induced reactions, $\pi^- p \rightarrow \eta n$, $K^0 \Lambda$, $K^+ \Sigma^-$, $K^0 \Sigma^0$, and $\pi^+ p \rightarrow K^+ \Sigma^+$. A detailed account of the data, listing also the weighting applied to different data sets, is given in Ref. [58]. The data base for $\gamma p \rightarrow \pi^0 p$ and $\pi^+ n$ used by JüBo is explained in Ref. [59], while the data taken into account for $\gamma p \rightarrow \eta p$ are listed in Ref. [60]. There, also the data on T and F from a recent MAMI measurement on η photoproduction [81] were included. Altogether almost 30,000 data points from photoproduction reactions were fitted. A complete account of the corresponding references can be found online [82]. The solution including all the mentioned data is named Fit B in Ref. [60].

BnGa: The BnGa group uses the amplitudes of the SAID WI08 energy-dependent solution and a comparable set of data on pion induced reactions as JüBo does. Furthermore, the data on $\pi^- p \rightarrow \pi^0 \pi^0 n$ are included. For photoproduction, the data base includes the reactions $\gamma p \rightarrow \pi N$, ηp , $K^+ \Lambda$, $K^+ \Sigma^0$, $K^0 \Sigma^+$, and three-body final states $2\pi^0 p$ [54, 55, 88, 89, 90, 91] and $\pi^0 \eta p$ [53]. The data sets used and the weights given to them in the fits are listed in [52, 92].

MAID: The MAID group uses data on photo- and electroproduction of $\pi^0 p$, $\pi^+ n$, and ηp available at the time when MAID2007 was reported [79]. The MAID homepage covers also KAON MAID [80]. Data on πN and ηp (and $K^+ \Lambda$) are fitted independently.

Particle properties: The SAID and MAID PWA groups use photoproduction reactions to determine the dynamics of the reaction and to determine the helicity amplitudes of contributing resonances while M_i , Γ_i , and BR_i^N are imposed from the fits to πN elastic scattering and

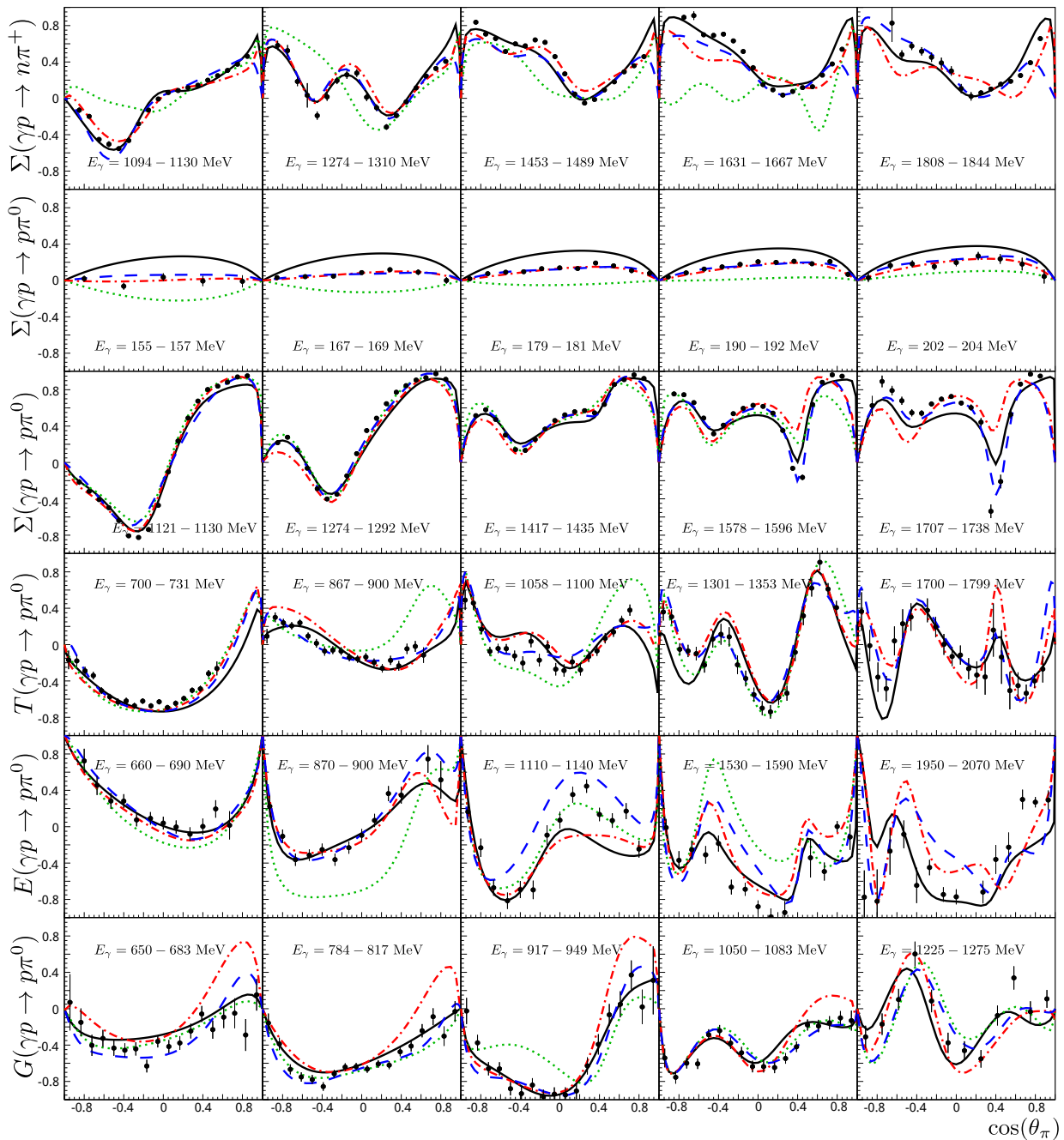


Fig. 1. Selected data and the predictions from the four different PWAs: black solid line: BnGa2011-02, blue dashed: JüBo2015B, green dotted: MAID2007, red dashed dotted: SAID CM12. The predictions are based on fits which did not yet use these new data. The new data are shown for the beam asymmetry Σ for $\gamma p \rightarrow \pi^+ n$ [95] (1st row), for the beam asymmetry Σ in the low-energy region [94] and at higher energies (2nd row) for $\gamma p \rightarrow \pi^0 p$, (2nd and 3rd row). The next three rows show T [96], G [38,97], and E [37,98] for $\gamma p \rightarrow \pi^0 p$. Note that the data from Refs. [94] and [95] are included in the fits of JüBo2015B and SAID CM12.

charge exchange reactions (SAID) or directly from the Review of Particle Properties, RPP, (MAID). The BnGa and JüBo groups use pion and photo-induced reactions and determine the properties of the contributing resonances in global fits to all included data.

New data: To study the impact of the new data from Bonn, JLab, and Mainz on the photoproduction multipoles, the PWA groups agreed to perform new fits incorporating the new data. In the fits called *predictions* below, the new data were (mostly) not yet included. The new fits took into account also the data listed in Table 1. The new fits, shown in Fig. 2, are all capable to reproduce the new

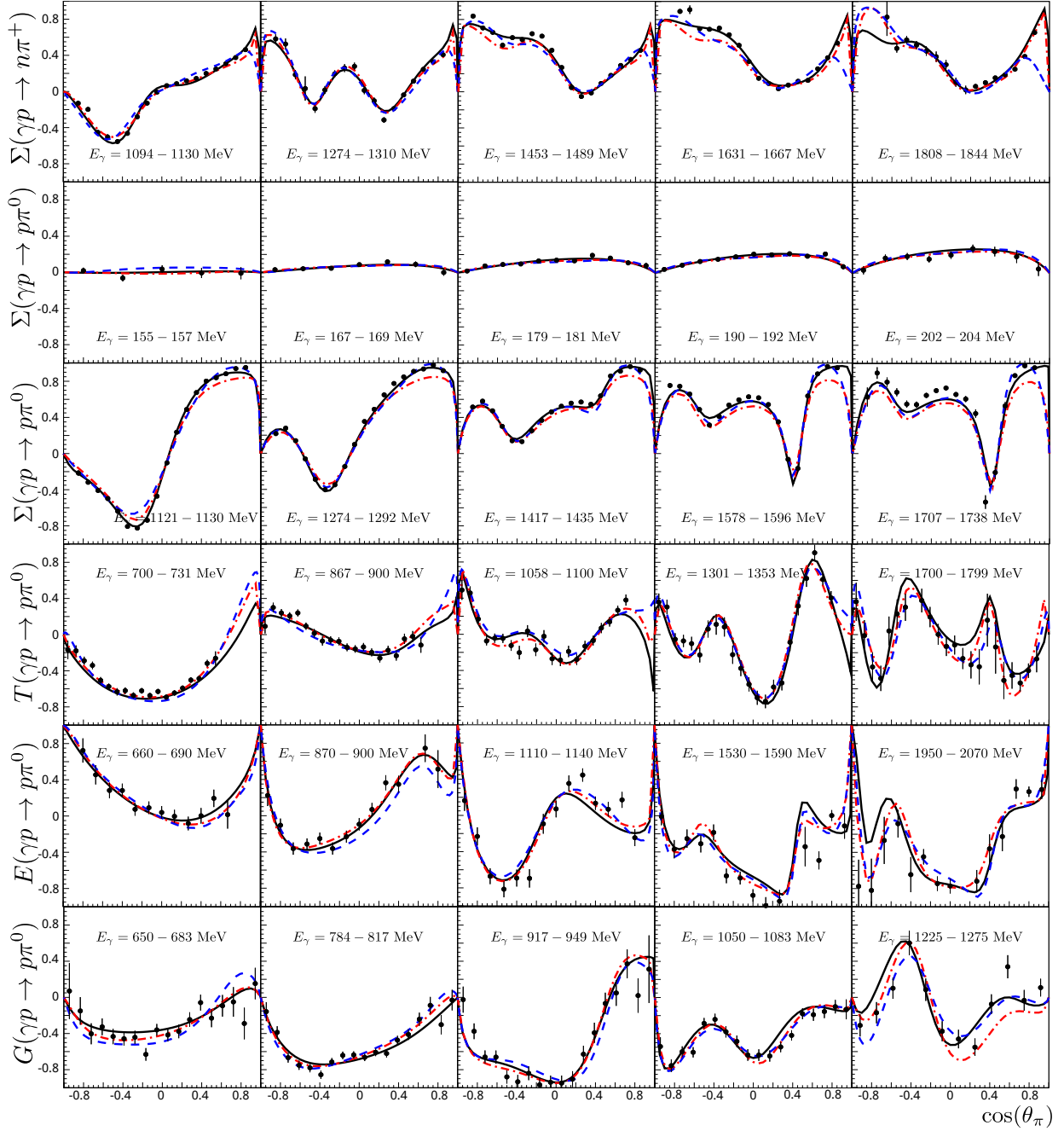


Fig. 2. The new fit results of the different PWAs in comparison with the new data: black solid line: BnGa, blue dashed: JüBo, red dashed dotted: SAID. New data are shown for the beam asymmetry Σ for $\gamma p \rightarrow \pi^+ n$ [95] (1st row), for the beam asymmetry Σ in the low-energy region [94] and at higher energies (2nd row) for $\gamma p \rightarrow \pi^0 p$, (2nd and 3rd row). The next three rows show T [96], G [38,97], and E [37,98] for $\gamma p \rightarrow \pi^0 p$. The BnGa fit did not yet use the data on the beam asymmetry Σ for $\gamma p \rightarrow \pi^0 p$ in the low-energy region [94]. Nevertheless, the new fit is fully consistent with the new data.

data reasonably well. This does, however, not imply that the multipoles resulting from these fits become identical. The partly still different data bases and differences in the formalism used to describe the new data may be responsible for the remaining differences in the multipoles shown in Figs. 3-6.

4 The photoproduction multipoles

In Figs. 3 - 6, the real and imaginary parts of the low- L^π multipoles for the photoproduction of pions from BnGa, JüBo, MAID, and SAID are presented. For BnGa, JüBo, and SAID the multipoles are shown from fits to data before and after the inclusion of the new data on polarization variables (see Table 1). The main aim of this section is to

Table 1. New data sets introduced recently into the PWA data bases and used for the new fits are marked with a \checkmark . Data marked with a \dagger were included already in the predictions (JüBo2015B and SAID CM12).

Reaction	Obs.	Range (MeV)	N_{data}	Ref.	BnGa	JüBo	SAID	Obs.	Range (MeV)	N_{data}	Ref.	BnGa	JüBo	SAID
$\gamma p \rightarrow \pi^0 p$	$d\sigma/d\Omega$	147 - 219	600	[94]	-	\dagger	\dagger	P, C_x, C_z	1845	1	[100]	-	-	\checkmark
	Σ	147 - 206	220	[94]	-	\dagger	\dagger	Σ	1102 - 1862	700	[95]	\checkmark	\dagger	\dagger
	T	684 - 1891	494	[96]	\checkmark	\checkmark	\checkmark	G	633 - 1300	318	[38,97]	\checkmark	\checkmark	\checkmark
	E	730 - 2100	455	[37,98]	\checkmark	\checkmark	\checkmark	C_x	463 - 1338	45	[99]	\checkmark	-	\checkmark
	P	684 - 917	158	[96]	\checkmark	\checkmark	\checkmark	H	684 - 917	158	[96]	\checkmark	\checkmark	\checkmark
$\gamma p \rightarrow \pi^+ n$	Σ	1112 - 1862	386	[95]	\checkmark	\dagger	\dagger							
$\gamma p \rightarrow K^+ \Lambda$	$d\sigma/d\Omega$			[101]	\checkmark	-	-							
$\gamma p \rightarrow K^+ \Sigma^0$	$d\sigma/d\Omega$			[101]	\checkmark	-	-							

demonstrate the impact of the new polarization data on the resulting multipoles.

For convenience, we recall in Table 2 the quantum numbers of the final πN state resulting from a given multipole. We also remind the reader that in case of a simple isolated Breit-Wigner resonance, the imaginary part of the multipole peaks at the nominal mass while the real part goes through zero.

4.1 The multipoles

The two reactions $\gamma p \rightarrow \pi^0 p$ and $\gamma p \rightarrow \pi^+ n$ can be described by multipoles in two different bases, in the physical channels, for example $E_{0+}(p\pi^0)$ and $E_{0+}(n\pi^+)$, or by the two isopin contributions, $I = 1/2$ leading to the nucleon resonances N^* and $I = 3/2$ leading to the Δ resonances Δ^* . In Figs. 3 - 6, we do not use an identical basis for all multipoles. For example, for the $\Delta(1232)3/2^+$ resonance we show the contributing multipoles M_{1+} and E_{1+} in the isospin basis $I = 3/2$ and $I = 1/2$. The $\Delta(1232)3/2^+$ resonance has an intrinsic quark spin $S = 3/2$. Hence one quark in the proton has to undergo a spin-flip, the driving multipole is a magnetic multipole M_{1+} , and the electric

Table 2. Photoproduction multipoles and partial waves. The partial waves are characterized by $L_{2I,2J}^\pi$, with L^π the orbital angular momentum, I the isospin and J the total spin of the πN system. In general, two multipoles belong to one spin-parity wave J^P .

Multipoles	L^π	πN partial waves		J^P	
		$I = 1/2$	$I = 3/2$		
E_{0+}	-	0	S_{11}	S_{31}	$1/2^-$
-	M_{1-}	1	P_{11}	P_{31}	$1/2^+$
E_{1+}	M_{1+}	1	P_{13}	P_{33}	$3/2^+$
E_{2-}	M_{2-}	2	D_{13}	D_{33}	$3/2^-$
E_{2+}	M_{2+}	2	D_{15}	D_{35}	$5/2^-$
E_{3-}	M_{3-}	3	F_{15}	F_{35}	$5/2^+$
E_{3+}	M_{3+}	3	F_{17}	F_{37}	$7/2^+$
E_{4-}	M_{4-}	4	G_{17}	G_{37}	$7/2^-$
E_{4+}	M_{4+}	4	G_{19}	G_{39}	$9/2^-$

multipole E_{1+} is very small. The same argument holds, e.g., for $N(1675)5/2^-$ where the contributing multipoles are the magnetic multipole M_{2+} and the electric multipole E_{2+} . The $N(1675)5/2^-$ has an intrinsic orbital angular momentum $L_q = 1$ (and at most very small components with higher angular momenta), hence its intrinsic quark spin must also be $S = 3/2$, and the relevant multipole driving the $N \rightarrow N(1675)5/2^-$ transition is a magnetic one, M_{2+} . Hence we present the multipoles in the isospin basis, $M_{2+}(I = 1/2)$ and $M_{2+}(I = 3/2)$. On the contrary, $N(1680)5/2^+$, excited by E_{3-} and M_{3-} , is a member of a spin doublet, with the $N(1720)3/2^+$ resonance as its spin partner. Here both, electric and magnetic multipoles contribute with similar magnitude, and we show the physical multipoles $M_{3-}(p\pi^0)$, $M_{3-}(n\pi^+)$ and $E_{3-}(p\pi^0)$, $E_{3-}(n\pi^+)$. The selection of the basis, isospin or physical channels, allows the reader to see the reaction-dependence of the different PWAs.

Figure 3 shows the E_{0+} multipole for the reactions $\gamma p \rightarrow \pi^0 p$ (a) and $\gamma p \rightarrow \pi^+ n$ (b). The multipole leads to πN in a relative S-wave. The real part of the $\gamma p \rightarrow \pi^+ n$ multipole reaches 40 mfm at threshold; the multipole is much smaller for $\gamma p \rightarrow \pi^0 p$. The sharp peak at low masses in $\pi^+ n$ is due to t -channel pion exchange which is forbidden for $\pi^0 p$ production. All three PWAs yield the same pattern: a strong threshold enhancement in $\gamma p \rightarrow \pi^+ n$ and a peak in the imaginary part of the multipole due to $N(1535)1/2^-$. The real part of the multipoles for $\pi^0 p$ and for $\pi^+ n$ production exhibits a sharp spike at the η production threshold. The multipoles show a very significant interference pattern between $N(1535)1/2^-$ and $N(1650)1/2^-$. The latter resonance is much more pronounced in the E_{0+} multipole for $\pi^+ n$ production. When the different PWA solutions are compared, it can be seen that the spread in the imaginary part of the multipole is reduced substantially when the new polarization data are taken into account. However, significant discrepancies remain, in particular in the low-mass region. The background contributions show a much wider spread than the resonant contributions. However, also the (small) $N(1650)1/2^-$ contributions differ in the different PWAs.

The M_{1-} multipole (Fig. 3c,d) drives the excitation of the $J^P = 1/2^+$ partial wave containing the Roper $N(1440)1/2^+$ resonance, the three-star $N(1710)1/2^+$ resonance, the one-star $\Delta(1750)1/2^+$, and the four-star $\Delta(1910)1/2^+$.

The imaginary part of the M_{1-} multipole evidences clearly $N(1440)1/2^+$, the contributions from the higher-mass resonances are small. The new data lead to a small improvement of the consistency of the results for the imaginary part of the multipole. In the real part a significant improvement can be observed.

The largest multipole is the $I = 3/2$ M_{1+} multipole (Fig. 3e), with the $\Delta(1232)3/2^+$ as the most prominent feature. The imaginary part peaks above 1200 MeV, and the real part goes through zero. In this mass region, the different methods gave already very similar predictions: very precise data and the Watson theorem were sufficient to determine the multipole reliably (if the latter is fulfilled). However, small discrepancies are seen above the $\Delta(1232)3/2^+$. The real part of the amplitude is slightly smaller in the BnGa analysis, this might be due to a small difference in the overall phase. It should be noted that BnGa includes the $\Delta(1600)3/2^+$ while in JüBo this state emerges as dynamically generated. Also the SAID approach finds a resonance pole in the corresponding energy region. The consistency of the four different analyses is hardly improved by the inclusion of the new data. The electric contribution, the E_{1+} multipole, is much smaller, see Fig. 4a. Also the $I = 1/2$ contributions to the M_{1+} and E_{1+} multipoles are small. The agreement between the different PWAs increased when the new polarization data were taken into account.

The E_{2-} and M_{2-} multipoles drive resonances with $J^P = 3/2^-$. The prominent peaks in the imaginary part of the amplitudes in Fig. 4 c-f are due to the $N(1520)3/2^-$. Its description by the different PWAs has converged to a nearly unique solution. Above, contributions are expected from $N(1700)3/2^-$, $\Delta(1700)3/2^-$, $N(1875)3/2^-$ (a new entry in the RPP and graded as three-star resonance), and $\Delta(1940)3/2^-$.

These four resonances contribute little to photoproduction of single pions, their main decay modes lead to $\pi\pi N$ final states. Their treatment is different in the different approaches, so it is understandable that the multipoles do not show a consistent behavior above 1600 MeV.

The M_{2+} and E_{2+} multipoles in Fig. 5 are again separated according to their isospin content. The imaginary part of the M_{2+} $I = 1/2$ multipole peaks at about 1700 MeV (Fig. 5b). The peak is due to the $N(1675)5/2^-$. In the quark model, this resonance has an intrinsic spin of $S = 3/2$, and hence the spin of one quark of the hit proton must flip. Thus we expect a dominant contribution from the magnetic multipole. This expectation is clearly met by the multipoles derived from the fits to the data. A second observation is that the spread of results from the different PWAs in the imaginary and real part of the M_{2+} multipole resonance is reduced visibly in the region of the $N(1675)5/2^-$ when the new polarization data are included in the fits, while the $I = 3/2$ background and the E_{2+} multipole have a large variance.

The multipoles M_{3-} and E_{3-} both show a clear resonant behavior due to photoexcitation of the $N(1680)5/2^+$ (Figs. 5e,f and 6a,b). We thus expect that the resonance must belong to a quark spin $S = 1/2$ doublet (with the

$N(1720)3/2^+$ as its spin partner). The consistency of the different PWA fits is rather good, and still improved with the new polarization data. In particular on the resonance position, the agreement between the different PWAs is excellent. In this case, the multipoles are shown in the particle base, the $\Delta(1905)5/2^+$ is hardly seen. Figure 7 shows the multipoles in the isospin basis. There is clear evidence for the $\Delta(1905)5/2^+$.

Figs. 6c,d show the $I = 3/2$ and $I = 1/2$ M_{3+} multipoles. The $I = 3/2$ M_{3+} multipole shows a very significant resonance, the $\Delta(1950)7/2^+$, which requires a quark spin flip. The electric E_{3+} multipole is correspondingly small and does not contain any evidence for a resonant structure. Likewise, the E_{4+} , M_{4+} – leading to $J^P = 9/2^+$ – and higher multipoles are small and their behavior is smooth.

The M_{4-} multipoles are small (Fig. 6e,f), E_{4-} (not shown) is even smaller. BnGa, JüBo, and GWU/SAID agree that the $N(2100)7/2^-$ resonance plays some role in photoproduction.

4.2 Consistency of the results

As one might expect, the four partial wave analyses yield different amplitudes. Ideally, the amplitudes should, in the limit of a complete data base with accurate data and full angular coverage, converge to the physical solution. In Fig. 8 the different amplitudes are compared. For this purpose, we calculate the variance between model 1 and 2 as

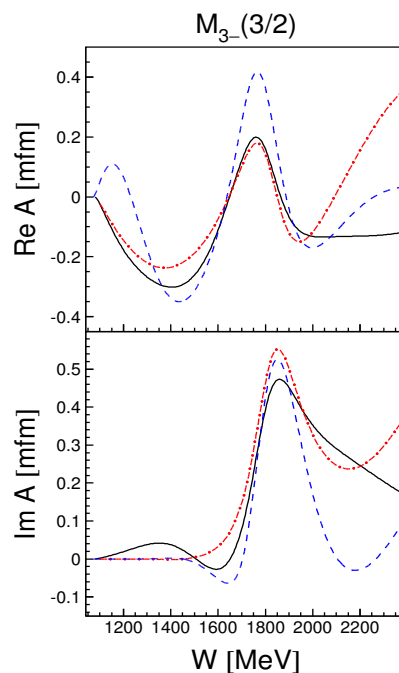


Fig. 7. The real and imaginary part of the M_{3-} multipole for $\gamma p \rightarrow \pi N$ after including the new data (black solid line: BnGa, blue dashed: JüBo, red dashed-dotted: SAID) evidences contributions from the $\Delta(1905)5/2^+$.

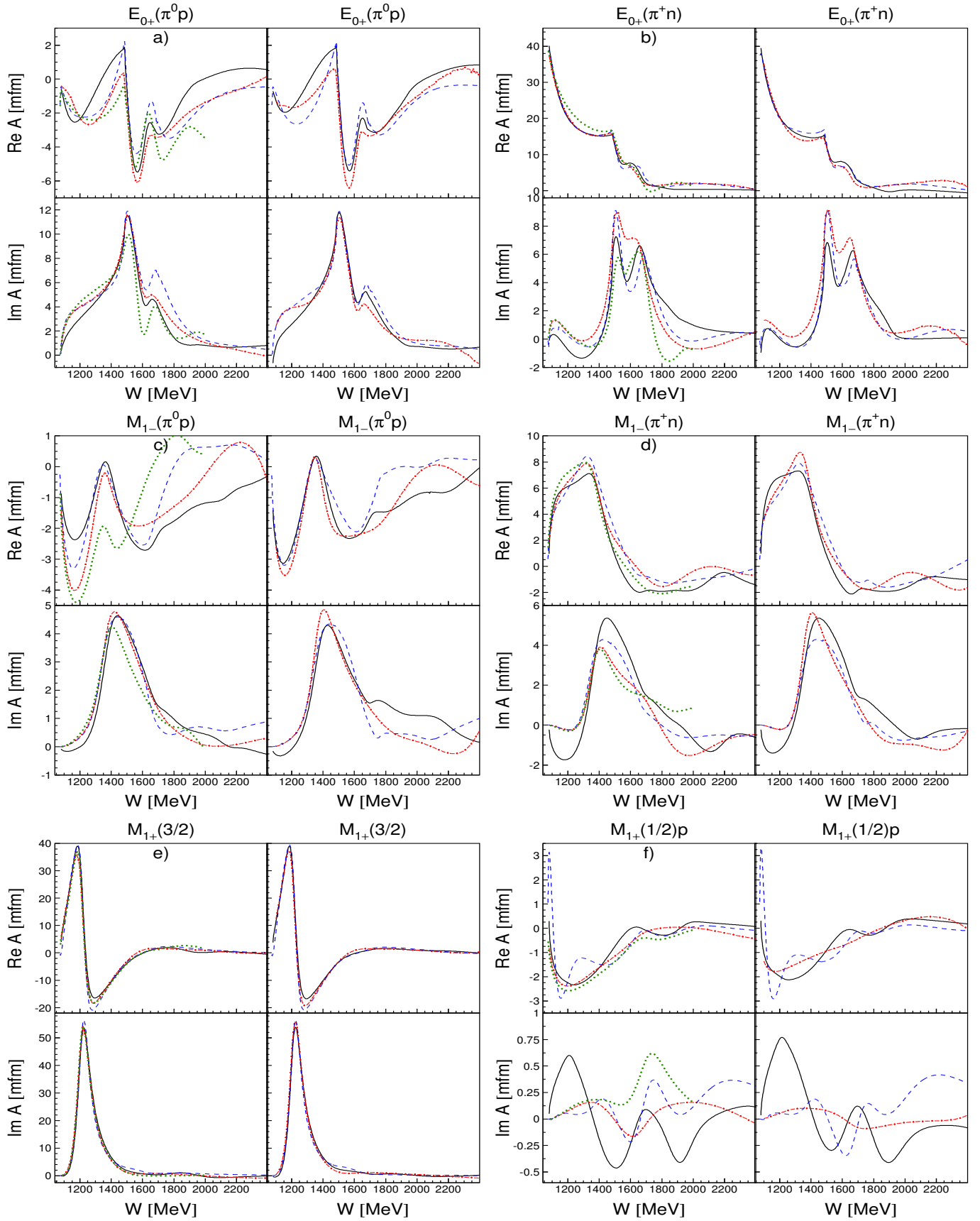


Fig. 3. Each block presents the real (top) and imaginary (bottom) part of multipoles for $\gamma p \rightarrow \pi N$, before (left) and after (right) including new data. Black solid line: BnGa, blue dashed: JüBo, red dashed dotted: SAID, green dotted: MAID. Blocks a and c show the $\gamma p \rightarrow \pi^0 p$ multipoles, b and d those for $\gamma p \rightarrow \pi^+ n$. Block e (f) presents the $I = 3/2$ ($I = 1/2$) multipoles.

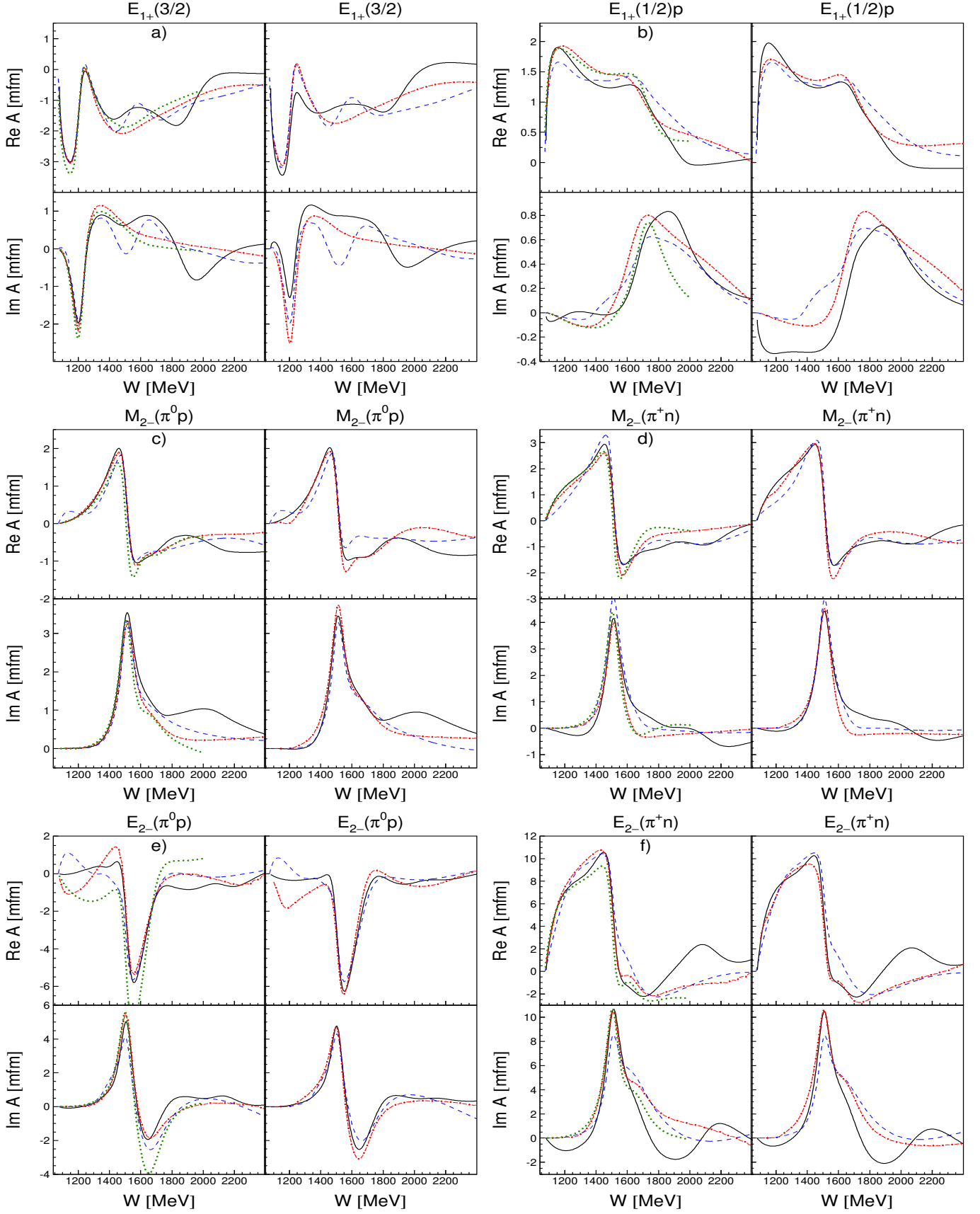


Fig. 4. Each block presents the real (top) and imaginary (bottom) part of multipoles for $\gamma p \rightarrow \pi N$, before (left) and after (right) including new data. Black solid line: BnGa, blue dashed: JüBo, red dashed dotted: SAID, green dotted: MAID. Block a (b) presents the $I = 3/2$ ($I = 1/2$) multipole; block c and e show the $\gamma p \rightarrow \pi^0 p$ multipoles, d and f those for $\gamma p \rightarrow \pi^+ n$.

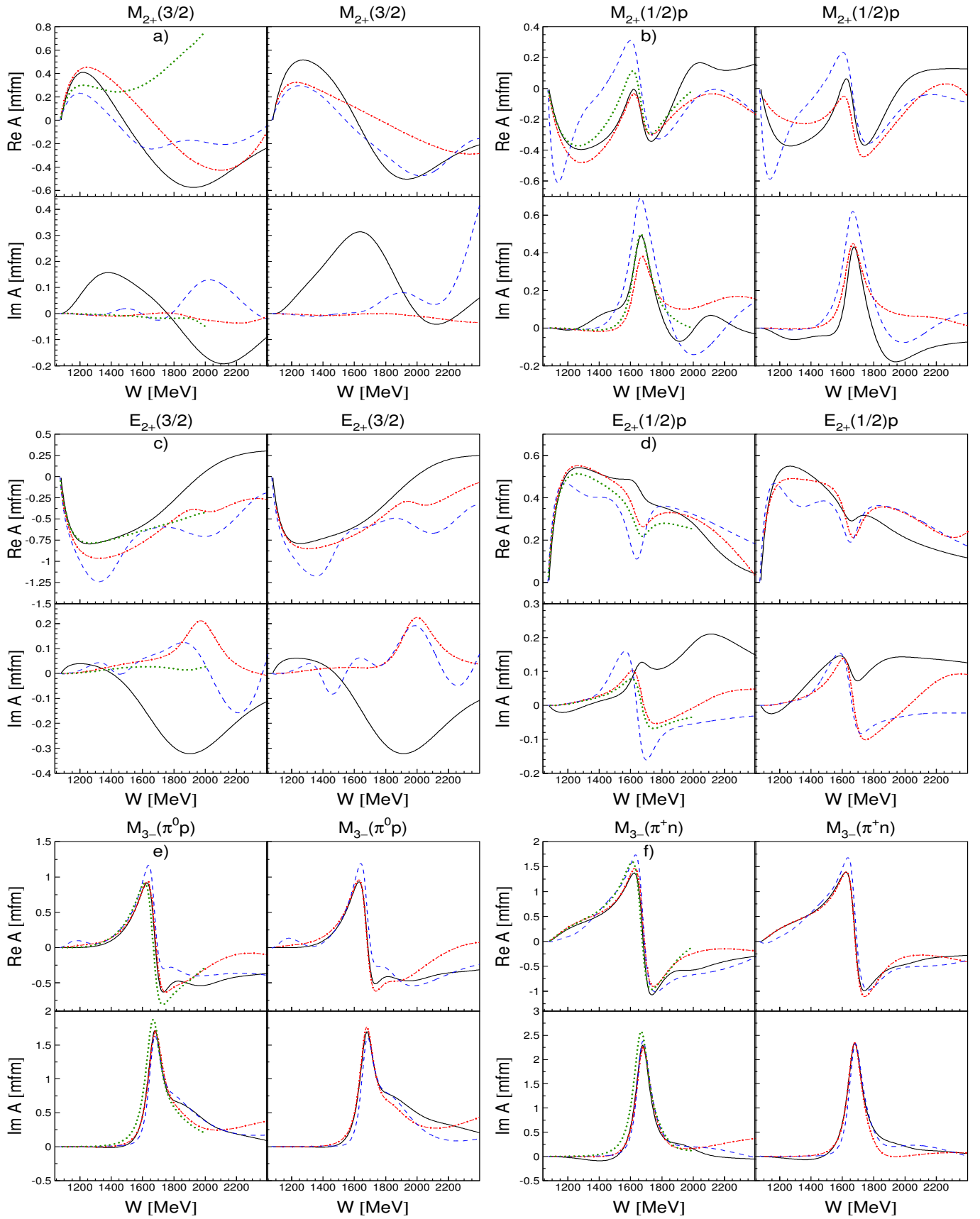


Fig. 5. Each block presents the real (top) and imaginary (bottom) part of multipoles for $\gamma p \rightarrow \pi N$, before (left) and after (right) including new data. Black solid line: BnGa, blue dashed: JüBo, red dashed dotted: SAID, green dotted: MAID. Blocks a and c (b and d) present the $I = 3/2$ ($I = 1/2$) multipoles; block e shows the $\gamma p \rightarrow \pi^0 p$ multipole, f that for $\gamma p \rightarrow \pi^+ n$.

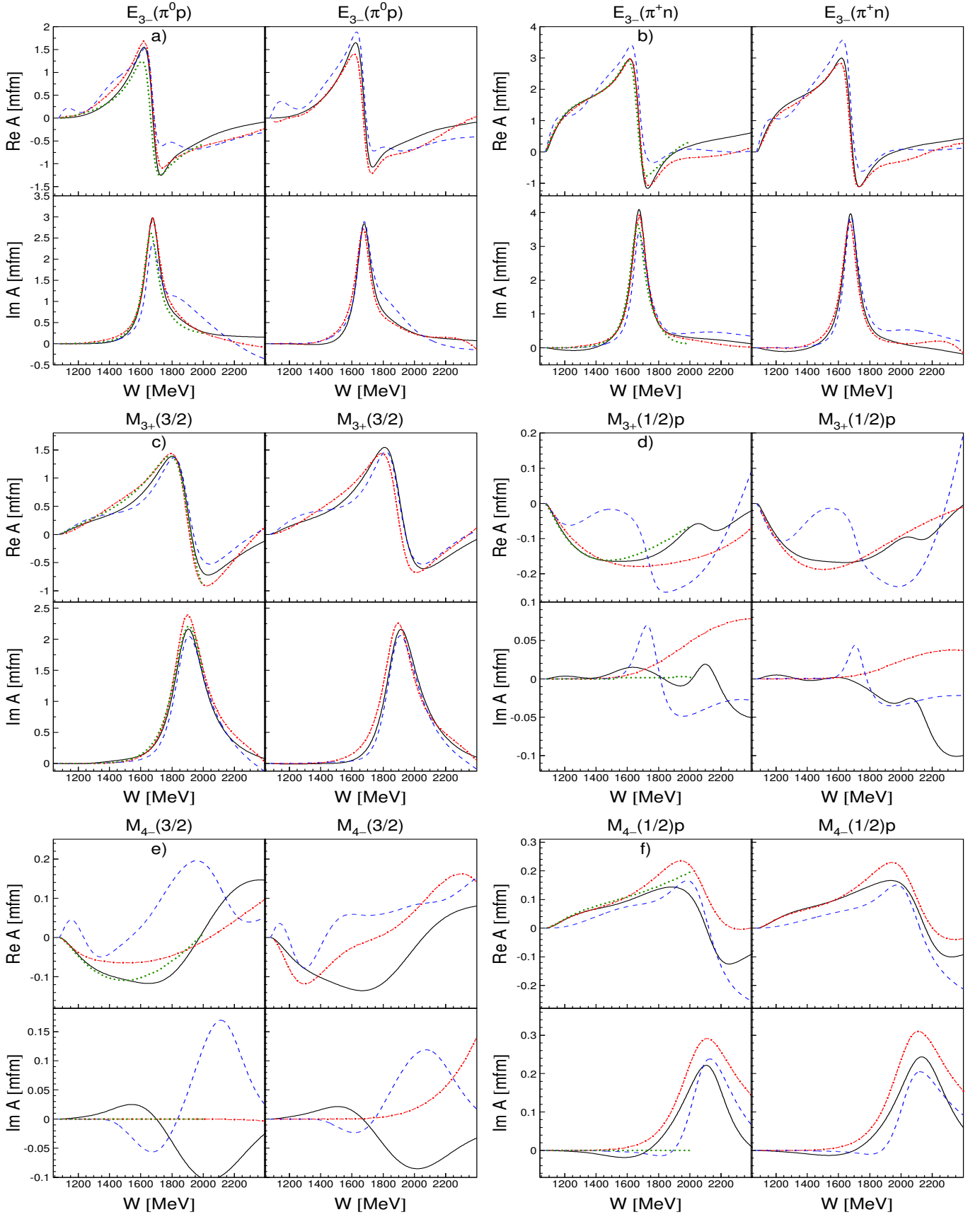


Fig. 6. Each block presents the real (top) and imaginary (bottom) part of multipoles for $\gamma p \rightarrow \pi N$, before (left) and after (right) including new data. Black solid line: BnGa, blue dashed: JüBo, red dashed dotted: SAID, green dotted: MAID. Block a shows the $\gamma p \rightarrow \pi^0 p$ multipole, b that for $\gamma p \rightarrow \pi^+ n$. Blocks c and e (d and f) present the $I = 3/2$ ($I = 1/2$) multipole.

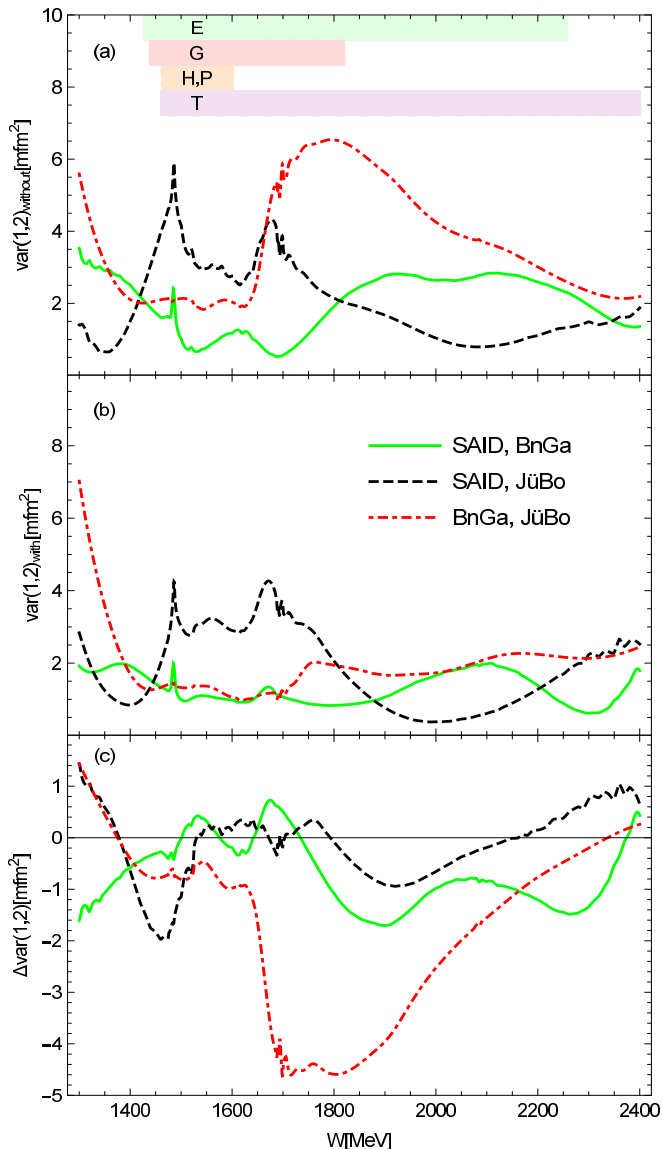


Fig. 8. The variances taken pairwise between two PWAs summed over all $\gamma p \rightarrow \pi^0 p$ multipoles up to $L = 4$. Solid (green): BnGa - SAID; dashed (black): SAID - JüBo; dashed-dotted (red): JüBo - BnGa. a: before including the new data, b: after including the new data, c: differences between a and b. The range covered by the new double polarization observables [96,97,98] is indicated by shaded areas.

the sum over the squared differences of the 16 (complex) $\gamma p \rightarrow \pi^0 p$ multipoles \mathcal{M} up to $L = 4$:

$$\text{var}(1, 2) = \frac{1}{2} \sum_{i=1}^{16} (\mathcal{M}_1(i) - \mathcal{M}_2(i)) (\mathcal{M}_1^*(i) - \mathcal{M}_2^*(i)). \quad (30)$$

This quantity is plotted in Fig. 8a for the amplitudes before and in Fig. 8b for the amplitudes after the new data were included. The spike in Fig. 8a slightly below $W = 1.5 \text{ GeV}$ reflects the discrepancies in the description of the ηp cusp between the approaches. Indeed, this is also directly visible for E_{0+} shown in Fig. 3. Once the

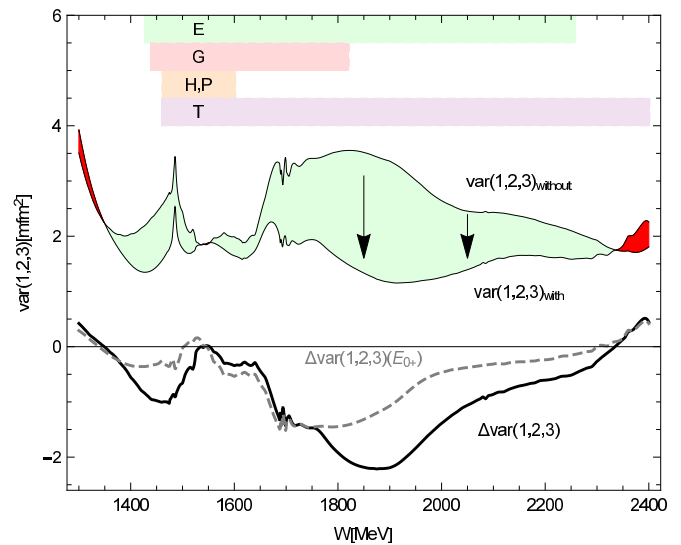


Fig. 9. The variance of all three PWAs summed over all $\gamma p \rightarrow \pi^0 p$ multipoles up to $L = 4$. The range covered by the new double polarization observables are indicated by shaded areas. Over the largest part of the energy range the new data have enforced an improvement of the overall consistency. The improvement is displayed as light green area and, separately as difference of the variance. The contribution to the improvement from the E_{0+} wave is shown as the dashed curve. Ranges with an overall deterioration are marked in red.

new data are included, this discrepancy becomes smaller (Fig. 8b). A wider peak below $W = 1.7 \text{ GeV}$ might stem from slightly different $N(1680)5/2^+$ properties used in the three PWAs. Also the wider peak becomes less pronounced when the new data are included in the fits. Large discrepancies are observed in the BnGa-JüBo comparison which are reduced very significantly in the new fits. Quite in general, all pairwise differences have become significantly smaller with the new data. With the new data included, the BnGa, JüBo, and SAID multipoles are now in closer agreement at energies beyond 1.7 GeV . In the region from 1500 to 1700 MeV , the BnGa prediction falls in between the JüBo and SAID predictions, thus BnGa agrees well with JüBo and SAID while a larger discrepancy remains between the latter two models. The improvement can be made visible in a figure (Fig. 8c) which displays the difference between Figs. 8a and b: it shows negative values indicating that the situation has been improved.

Figure 9 shows the reduction of the overall spread of the three partial wave analyses. Overall this spread is reduced considerably due to the impact of the new polarization variables [96,97,98]. A significant fraction of the improvement stems from the E_{0+} multipole exciting the $J^P = 1/2^-$ wave (and thus the resonances $N(1535)$, $\Delta(1620)$, $N(1650)$, $N(1895)$, and $\Delta(1900)$).

5 Summary and conclusions

We have presented a comparison of the multipoles derived from data on pion photoproduction in four differ-

ent partial wave analyses performed by the groups Bonn-Gatchina (BnGa), Jülich-Bonn (JüBo), MAID from Mainz, and SAID from GWU. We have compared the multipoles from fits made before new polarization data became available and from fits which included the new data in the fitted data base. We find that the new data force the multipoles to get closer to each other, the variance is reduced by about a factor of two.

Even more important seems to be that the multipoles converge to similar values in the region of leading resonances while the “background” and the contribution of higher-mass resonances remain less constrained by the new data. Clearly, the aim is to get very similar answers also in the mass range which contains higher-mass resonances. This task will require more precise data, in particular more precise data on polarization observables.

Acknowledgements: This work was supported by the DFG (SFB/TR 16, SFB 1044, and the Sino-German CRC 110), the Department of Energy (Offices of Science and Nuclear Physics) award no. DE-FG02-99-ER41110, the National Science Foundation through the NSF/PIF grant No. PHY 1415459, NSF/Career grant No. 1452055 and the Chinese Academy of Sciences (CAS) President’s International Fellowship Initiative (PIFI) (Grant No. 2015VMA076). M. D., U.-G. M. and D. R. gratefully acknowledge the computing time granted on the supercomputer JURECA at the Jülich Supercomputing Centre (JSC). A.V.A., V.N. and A.S. acknowledge the support from RSF grant 16-12-10267.

References

1. V. Crede and C. A. Meyer, *Prog. Part. Nucl. Phys.* **63**, 74 (2009).
2. E. Klempt and A. Zaitsev, *Phys. Rept.* **454**, 1 (2007).
3. K. A. Olive *et al.* [Particle Data Group Collaboration], *Chin. Phys. C* **38**, 090001 (2014).
4. S. Capstick and N. Isgur, *Phys. Rev. D* **34**, 2809 (1986).
5. U. Löring, B. C. Metsch, and H. R. Petry, *Eur. Phys. J. A* **10**, 395 (2001).
6. M. M. Giannini and E. Santopinto, *Chin. J. Phys.* **53**, 020301 (2015).
7. R. G. Edwards, J. J. Dudek, D. G. Richards, and S. J. Wallace, *Phys. Rev. D* **84**, 074508 (2011).
8. G. P. Engel *et al.* [BGR Collaboration], *Phys. Rev. D* **87**, no. 7, 074504 (2013).
9. C. B. Lang and V. Verduci *Phys. Rev. D* **87**, no. 5, 054502 (2013).
10. S. Capstick and P. R. Page, *Phys. Rev. C* **66**, 065204 (2002).
11. J. J. Dudek and R. G. Edwards, *Phys. Rev. D* **85**, 054016 (2012).
12. M. Anselmino, E. Predazzi, S. Ekelin, S. Fredriksson, and D. B. Lichtenberg, *Rev. Mod. Phys.* **65**, 1199 (1993).
13. N. Kaiser, P. B. Siegel and W. Weise, *Phys. Lett. B* **362**, 23 (1995).
14. U.-G. Meißner and J. A. Oller, *Nucl. Phys. A* **673**, 311 (2000).
15. E. E. Kolomeitsev and M. F. M. Lutz, *Phys. Lett. B* **585**, 243 (2004).
16. S. Sarkar, B. X. Sun, E. Oset, and M. J. Vicente Vacas, *Eur. Phys. J. A* **44**, 431 (2010).
17. E. Oset and A. Ramos, *Eur. Phys. J. A* **44**, 445 (2010).
18. P. C. Bruns, M. Mai and U.-G. Meißner, *Phys. Lett. B* **697**, 254 (2011).
19. H. Forkel and E. Klempt, *Phys. Lett. B* **679**, 77 (2009).
20. G. F. de Teramond, H. G. Dosch, and S. J. Brodsky, *Phys. Rev. D* **91**, no. 4, 045040 (2015).
21. E. Klempt, *Chin. Phys. C* **34**, no. 9, 1241 (2010).
22. J. Segovia, I. C. Cloet, C. D. Roberts, and S. M. Schmidt, *Few Body Syst.* **55**, 1185 (2014).
23. C. D. Roberts, arXiv:1509.08952 [nucl-th].
24. E. Klempt and J. M. Richard, *Rev. Mod. Phys.* **82**, 1095 (2010).
25. E. Klempt and B. C. Metsch, *Eur. Phys. J. A* **48**, 127 (2012).
26. V. Crede and W. Roberts, *Rept. Prog. Phys.* **76**, 076301 (2013).
27. W. Plessas, *Int. J. Mod. Phys. A* **30**, no. 02, 1530013 (2015).
28. <http://wwwnew.hiskp.uni-bonn.de/cb/>.
29. <http://wwwa2.kph.uni-mainz.de/>.
30. <https://www.jlab.org/Hall-B/>.
31. I. S. Barker, A. Donnachie, and J. K. Storrow, *Nucl. Phys. B* **95**, 347 (1975).
32. W. T. Chiang and F. Tabakin, *Phys. Rev. C* **55**, 2054 (1997).
33. C. G. Fasano, F. Tabakin, and B. Saghai, *Phys. Rev. C* **46**, 2430 (1992).
34. Y. Wunderlich, R. Beck, and L. Tiator, *Phys. Rev. C* **89**, no. 5, 055203 (2014).
35. R. Beck *et al.*, *Phys. Rev. Lett.* **78**, 606 (1997).
36. G. Blanpied *et al.*, *Phys. Rev. Lett.* **79**, 4337 (1997).
37. M. Gottschall *et al.* [CBELSA/TAPS Collaboration], *Phys. Rev. Lett.* **112**, 012003 (2014).
38. A. Thiel *et al.* [CBELSA/TAPS Collaboration], *Phys. Rev. Lett.* **109**, 102001 (2012).
39. J. Hartmann *et al.*, *Phys. Rev. Lett.* **113**, 062001 (2014).
40. A. S. Omelaenko, *Yad. Fiz.* **34**, 730 (1981).
41. V. F. Grushin, in *Photoproduction of Pions on Nucleons and Nuclei*, A. A. Komar (eds.) (Nova Science, New York, 1989), p. 1ff.
42. R. L. Workman, L. Tiator and A. Sarantsev, *Phys. Rev. C* **87**, 068201 (2013).
43. H. Kamano, S. X. Nakamura, T.-S. H. Lee, and T. Sato, *Phys. Rev. C* **87**, 015201 (2013), *C* **88**, 035209 (2013).
44. V. Shklyar, H. Lenske, and U. Mosel, *Phys. Rev. C* **86**, 055203 (2012).
45. M. Shrestha and D. M. Manley, *Phys. Rev. C* **86**, 055203 (2012).
46. A. V. Anisovich, E. Klempt, A. V. Sarantsev, U. Thoma, *Eur. Phys. J. A* **24**, 111 (2005).
47. A. V. Anisovich and A. V. Sarantsev, *Eur. Phys. J. A* **30**, 427 (2006).
48. A. V. Anisovich, E. Klempt, V. A. Nikonov, M. A. Matveev, A. V. Sarantsev, and U. Thoma, *Eur. Phys. J. A* **44**, 203 (2010).
49. S. U. Chung, J. Brose, R. Hackmann, E. Klempt, S. Spanier, and C. Strassburger, *Annalen Phys.* **4**, 404 (1995).
50. R. A. Arndt, W. J. Briscoe, I. I. Strakovsky, and R. L. Workman, *Phys. Rev. C* **74**, 045205 (2006).
51. V. V. Anisovich, M. A. Matveev, V. A. Nikonov, J. Nyiri, and A. V. Sarantsev, Hackensack, USA: World Scientific (2008) 580 p.

52. A. V. Anisovich, R. Beck, E. Klempt, V. A. Nikonov, A. V. Sarantsev, and U. Thoma, *Eur. Phys. J. A* **48**, 15 (2012).
53. E. Gutz *et al.* [CBELSA/TAPS Collaboration], *Eur. Phys. J. A* **50**, 74 (2014).
54. V. Sokhoyan *et al.* [CBELSA/TAPS Collaboration], *Eur. Phys. J. A* **51**, 95 (2015).
55. V. Sokhoyan *et al.* [CBELSA/TAPS Collaboration], *Phys. Lett. B* **746**, 127 (2015).
56. A. Thiel *et al.* [CBELSA/TAPS Collaboration], *Phys. Rev. Lett.* **114**, no. 9, 091803 (2015).
57. M. Döring, C. Hanhart, F. Huang, S. Krewald, U.-G. Meißner, and D. Rönchen, *Nucl. Phys. A* **851**, 58 (2011).
58. D. Rönchen, M. Döring, F. Huang, H. Haberzettl, J. Haidenbauer, C. Hanhart, S. Krewald, U.-G. Meißner, and K. Nakayama, *Eur. Phys. J. A* **49**, 44 (2013).
59. D. Rönchen, M. Döring, F. Huang, H. Haberzettl, J. Haidenbauer, C. Hanhart, S. Krewald, U.-G. Meißner, and K. Nakayama, *Eur. Phys. J. A* **50**, 101 (2014).
60. D. Rönchen, M. Döring, H. Haberzettl, J. Haidenbauer, U.-G. Meißner, and K. Nakayama, *Eur. Phys. J. A* **51**, 70 (2015).
61. C. Schütz, J. Haidenbauer, J. Speth, and J. W. Durso, *Phys. Rev. C* **57**, 1464 (1998).
62. M. Döring, C. Hanhart, F. Huang, S. Krewald, and U.-G. Meißner, *Nucl. Phys. A* **829**, 170 (2009).
63. S. Ceci, M. Döring, C. Hanhart, S. Krewald, U.-G. Meißner, and A. Švarc, *Phys. Rev. C* **84**, 015205 (2011).
64. R. Aaron, R. D. Amado, and J. E. Young, *Phys. Rev.* **174**, 2022 (1968).
65. C. Schütz, J. W. Durso, K. Holinde, and J. Speth, *Phys. Rev. C* **49**, 2671 (1994).
66. F. Huang, M. Döring, H. Haberzettl, J. Haidenbauer, C. Hanhart, S. Krewald, U.-G. Meißner, and K. Nakayama, *Phys. Rev. C* **85**, 054003 (2012).
67. L. Tiator, D. Drechsel, S. S. Kamalov, and M. Vanderhaeghen, *Eur. Phys. J. ST* **198**, 141 (2011)
68. V. Bernard, N. Kaiser, J. Gasser, U.-G. Meißner, *Phys. Lett.* **B268**, 291 (1991).
69. S. S. Kamalov, G.-Y. Chen, S.-N. Yang, D. Drechsel, L. Tiator, *Phys. Lett.* **B522**, 27 (2001).
70. D. Drechsel, O. Hanstein, S. S. Kamalov, and L. Tiator, *Nucl. Phys. A* **645**, 145 (1999).
71. D. Drechsel, S. S. Kamalov, and L. Tiator, *Eur. Phys. J. A* **34**, 69 (2007); <http://www.kph.uni-mainz.de/MAID/>.
72. R. A. Arndt, I. I. Strakovsky, R. L. Workman, *Phys. Rev. C* **53** (1996) 430-440; (SP99 solution of the GW/SAID analysis); <http://gwdac.phys.gwu.edu/>.
73. R. L. Workman, *Phys. Rev. C* **74**, 055207 (2006).
74. R. L. Workman, M. W. Paris, W. J. Briscoe, and I. I. Strakovsky, *Phys. Rev. C* **86**, 015202 (2012).
75. R. L. Workman, R. A. Arndt, W. J. Briscoe, M. W. Paris, and I. I. Strakovsky, *Phys. Rev. C* **86**, 035202 (2012).
76. M. W. Paris and R. L. Workman, *Phys. Rev. C* **82**, 035202 (2010).
77. R. A. Arndt, J. M. Ford, and L. D. Roper, *Phys. Rev. D* **32**, 1085 (1985).
78. The SAID database can be access from <http://said.phys.gwu.edu..>
79. D. Drechsel, S. S. Kamalov, and L. Tiator, *Eur. Phys. J. A* **34**, 69 (2007).
80. T. Mart and C. Bennhold, *Phys. Rev. C* **61**, 012201 (2000).
81. C. S. Akondi *et al.* [A2 at MAMI Collaboration], *Phys. Rev. Lett.* **113**, no. 10, 102001 (2014).
82. The full photoproduction data base of the Jülich2015 analysis is available at http://collaborations.fz-juelich.de/ikp/meson-baryon/juelich_amplitudes.html.
83. M. Dugger *et al.*, *Phys. Rev. C* **76**, 025211 (2007).
84. M. Dugger *et al.*, *Phys. Rev. C* **79**, 065206 (2009).
85. J. Ahrens *et al.*, *Eur. Phys. J. A* **21**, 323 (2004).
86. J. Ahrens *et al.*, *Phys. Rev. C* **74**, 045204 (2006).
87. R. Beck, *Eur. Phys. J. A* **28S1**, 173 (2006).
88. U. Thoma *et al.* [CBELSA Collaboration], *Phys. Lett. B* **659**, 87 (2008).
89. A. V. Sarantsev *et al.*, *Phys. Lett. B* **659**, 94 (2008).
90. Y. Assafiri *et al.*, *Phys. Rev. Lett.* **90**, 222001 (2003).
91. V. L. Kashevarov *et al.* [Crystal Ball at MAMI, TAPS, and A2 Collaborations], *Phys. Rev. C* **85**, 064610 (2012).
92. A. V. Anisovich, E. Klempt, V. A. Nikonov, A. V. Sarantsev, and U. Thoma, *Eur. Phys. J. A* **49**, 158 (2013).
93. S. Prakhov *et al.* [Crystal Ball Collaboration], *Phys. Rev. C* **69**, 045202 .
94. D. Hornidge *et al.* [A2 and CB-TAPS Collaborations], *Phys. Rev. Lett.* **111**, no. 6, 062004 (2013).
95. M. Dugger *et al.* [CLAS Collaboration], *Phys. Rev. C* **88**, no. 6, 065203 (2013) [*Phys. Rev. C* **89**, no. 2, 029901 (2014)].
96. J. Hartmann *et al.* [CBELSA/TAPS Collaboration], *Phys. Lett. B* **748**, 212 (2015).
97. A. Thiel *et al.* [CBELSA/TAPS Collaboration], “Double-polarization observable G in neutral-pion photoproduction”, arXiv:1604.02922 [nucl-ex].
98. M. Gottschall *et al.* [CBELSA/TAPS Collaboration], “Double-polarization observable E in neutral-pion photoproduction”, in preparation.
99. M. H. Sikora *et al.*, *Phys. Rev. Lett.* **112**, no. 2, 022501 (2014).
100. W. Luo *et al.*, *Phys. Rev. Lett.* **108**, 222004 (2012).
101. T. C. Jude *et al.* [Crystal Ball at MAMI Collaboration], *Phys. Lett. B* **735**, 112 (2014).